Subsurface Radar Imaging by Optimizing Sensor Locations in Spatio-Spectral Domains

Chandan Bhat, Maria Antonia Maisto, Uday K. Khankhoje, *Senior Member, IEEE*, and Raffaele Solimene, *Senior Member, IEEE*

Abstract—This paper deals with subsurface radar imaging for a two-dimensional scalar setting consisting of a two-layered background medium imaged via a multi-frequency, multi-monostatic configuration. The objective is to reduce data for a subsurface imaging problem without performance degradation by determining the optimal sensor locations in both spatial and frequency domains. In this regard, we present a sampling method that effectively extends the Maximal Projection on Minimum Eigenspace (MPME) algorithm to tackle the semi-discrete inverse problem associated with subsurface imaging. Compared to the state-of-the-art technique, we significantly reduce the required samples for imaging. Numerical and experimental results, the latter concerning a buried water pipe, are reported to demonstrate the effectiveness of the proposed sampling strategy. In particular, for the considered cases, the proposed sampling method shows a data reduction of more than 50% compared to other literature sampling methods.

Index Terms—Subsurface Imaging, Ground Penetrating Radars, Inverse Imaging, Sensor Selection.

I. Introduction

Subsurface radar imaging (SRI) is a mature research field relevant to countless applications (for example, [1]–[7]). From a mathematical point of view, imaging entails inverting a linearized approximation of the scattering operator [8], [9], with the achievable performance depending on the configuration parameters [10] (measurement aperture [11], frequency band [12] and background medium [13]), the noise level and the employed inversion algorithm [14].

The procedure and the amount of data collection are crucial. Indeed, too much data does not necessarily improve performance and can waste resources. In contrast, inadequate data can lead to aliasing artifacts that can be mistaken as actual targets. Thus, it is of great interest to devise a sampling scheme that demands as low data as possible to achieve the twin goals of (i) reducing data acquisition time and storage resources and (ii) speeding up imaging algorithms while controlling the achievable performance.

This paper considers a two-dimensional (2D) scalar geometry and a two-layered background medium with a multi-frequency, multi-monostatic configuration. This is a common way to describe a slice of the subsurface imaging problem.

Determining the measurement positions and the frequencies (number and arrangement) is a way to discretize the range

C. Bhat and U. K. Khankhoje are with the Department of Electrical Engineering, Indian Institute of Technology Madras, Chennai, India.

M. A. Maisto and R. Solimene are with the Dipartimento di Ingegneria, Università della Campania Luigi Vanvitelli, Aversa, Italy.

C. Bhat (corresponding author, e-mail: chandanbhat21@gmail.com)

of the scattering operator. Hence, a natural approach for data sampling is to estimate the filtering introduced by the scattering operator and then employ the Nyquist criterion to sample the data. The band of the scattered data can be estimated by resorting to the plane-wave expansion of the relevant Green function kernel. For a monostatic configuration (once evanescent waves are neglected), the field can be uniformly sampled at $\lambda_{umin}/4$, with λ_{umin} being the wavelength corresponding to the highest employed frequency in the free-space. This approach leads to a huge oversampling. A better estimation is usually obtained by invoking stationary phase arguments [15]–[17]. However, this approach still leads to an unnecessarily high number of data, especially for near-field configuration, large measurement aperture, and spatial region to be imaged. Recent results concerning the so-called warping [18]–[20] method consider the varying nature of the field spatial band (i.e., the support of the scattered field Fourier transformation with respect to the measurement location) and have shown that the number of data can be dramatically reduced by non-uniform sampling. However, frequencies are still uniformly sampled, and spatial positions are determined in correspondence with only the highest frequency and used for all the employed frequencies.

The previous discussion highlights that there is still room for data reduction. This requires a sampling criterion that selects the frequencies and optimizes spatial positions for each retained frequency. Unfortunately, analytical arguments at the base of the warping method have yet to be developed for this case.

Data sampling can be cast as a sensor selection problem [21] to cope with this lack. However, sensor selection is an NP-hard problem. To avoid exponential complexity, convex optimization [22], and several greedy algorithms have been proposed in the literature [23]–[25]. These procedures sequentially enlarge the set of data according to some figure of merit (related to the noise and the singular values of the incremental model), which has to satisfy certain constraints accounting for the propagation of noise from data to reconstructions. Among them, Maximal Projection on Minimum Eigenspace (MPME) [26] offers some advantages and hence has been selected herein. However, MPME is conceived for matrix problems (i.e., both data and unknowns have finite dimensions) with the number of unknowns fixed in advance. Data selection is achieved by running an iterative procedure, which needs a singular value decomposition (SVD) computation at each step. Therefore, it is not well suited to deal with the problem at hand. Indeed, even though imaging entails solving a matrix

problem since the unknowns belong to continuous function space, the discretized matrix model is generally very large in size (unless a priori information about the unknown scene is available) and the MPME is computationally heavy and resource demanding. This, for example, happens when pixel-based functions are employed to represent the unknown. Moreover, classical MPME stops when the number of selected data exceeds the number of unknowns. Consequently, when the number of unknowns is large, the required data is even larger, which is inconvenient for imaging problems.

To avoid this drawback, we appropriately modify the MPME algorithm:

1) The unknowns are projected on the "essential" singular functions of the scattering operator (i.e., the ones that mainly contribute), approximated by a finely discretized matrix model. Hence, this drastically reduces the problem's size and partially regularizes the related inverse problem.

2) We propose a new stopping rule based on a lower bound of the trace of the pseudoinverse of the incremental model, which allows us to stop the iteration before the number of data exceeds the unknowns.

These modifications avoid the SVD computation at each iteration.

The rest of the paper is organized as follows. Section II describes the problem and the related necessary notations. Section III provides the context for this paper. To this end, the sampling strategy and the classical MPME are briefly recalled. In Section IV, the proposed method is introduced. The reconstruction algorithms are briefly sketched in Section V, whereas numerical and experimental results are presented in Sections V and VI, respectively. In particular, experiments refer to actual on-site data concerning a buried pipe. Finally, the discussion and conclusions end the paper.

II. PROBLEM DESCRIPTION

Consider the two-dimensional (2D) scalar subsurface scattering scenario shown in Fig. 1. Invariance is assumed along the y direction, whereas the interface at $z = 0$ splits the entire $x - z$ plane into two half-spaces. The upper half ($z > 0$) is free-space with dielectric permittivity $\epsilon_u = \epsilon_0$ and the lower half ($z \leq 0$) consists of a non-magnetic medium with dielectric permittivity $\epsilon_l = \epsilon_r \epsilon_0$ ($\epsilon_r > 0$).

Targets are assumed to reside within the rectangular scattering domain $SD = [x_{min}, x_{max}] \times [z_{min}, z_{max}]$, embedded in the lower half-space, whereas scattered field data are collected according to a multi-monostatic configuration over a line segment, i.e., the observation domain (OD), along the x axis varying from $-x_s$ to x_s at a height $z_o > 0$. The source emits a y-polarized incident field with unit amplitude for frequencies within the wavenumber band $k_0 \in \Omega = [k_{min}, k_{max}]$, with k_0 being the wavenumber in free-space. The scattered field at a given data point $(x_o, k_0) \in \Sigma = OD \times \Omega$ is expressed by a first kind Fredholm integral equation, that, under the Born approximation [27] reads as:

$$E^s(x_o, k_0) = jk_l^2 \omega \mu_0 \int_{SD} G^2(x_o, \vec{r}, k_0)\chi(\vec{r})d\vec{r}, \quad (1)$$
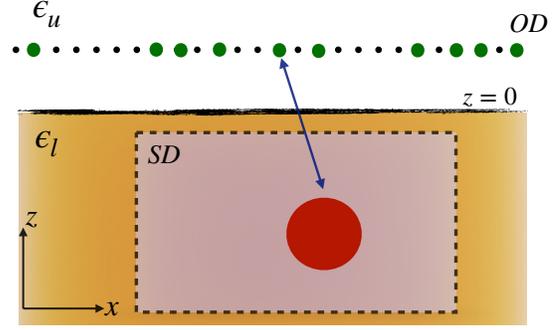

Fig. 1: Schematic of the mono-static subsurface scattering configuration. A scatterer with unknown position and permittivity is shown in red within the scattering domain (SD), while the green dots denote the measurement locations in the observation domain (OD).

where $E^s(\cdot)$ is the scattered field, k_l is the wavenumber in the lower half-space, ω the angular frequency, μ_0 the magnetic permeability of freespace, $\chi(\vec{r}) = \epsilon_r^t(\vec{r}) - 1$ is the target contrast function, with $\epsilon_r^t(\vec{r})$ being the relative (with respect to the lower half-space) target dielectric permittivity, and $G(\cdot)$ is the half-space Green function approximated from the well-known Weyl expansion [28]. Note that the Green function appears squared because of the monostatic configuration considered.

Equation (1) can be conveniently represented in operator notation as

$$\mathcal{A} : \chi \in L^2(SD) \longrightarrow \mathbf{E}^s \in \mathbb{C}^{N_p \times N_f}(\Sigma), \quad (2)$$

where $\mathcal{A}$ is the semi-discrete linear integral operator in (1) that links square integrable functions supported over SD to complex matrices. In particular, $\mathbb{C}^{N_p \times N_f}(\Sigma)$ means the set of complex matrices obtained by sampling the scattered field over a $N_p \times N_f$ grid belonging to Σ, with N_p and N_f being the number of spatial positions and frequencies, respectively.

A. Over-sampled discrete operator

In order to proceed further, we need the complete discrete counterpart of $\mathcal{A}$. To this end, a uniform $N_p \times N_f$ grid of Σ is considered to sample the data, whereas SD is discretized into $N \times N$ bins. Accordingly, the following matrix model is obtained as:

$$\underbrace{\begin{bmatrix} \mathbf{A}_1 \\ \mathbf{A}_2 \\ \vdots \\ \mathbf{A}_{N_f} \end{bmatrix}}_{\mathbf{A}} \begin{bmatrix} \boldsymbol{x} \end{bmatrix} = \underbrace{\begin{bmatrix} \boldsymbol{e}_1(x_{1:M}, k_{01}) \\ \boldsymbol{e}_2(x_{1:M}, k_{02}) \\ \vdots \\ \boldsymbol{e}_{N_f}(x_{1:M}, k_{0N_f}) \end{bmatrix}}_{\boldsymbol{e}} + \boldsymbol{\nu}, \quad (3)$$

where $\mathbf{A}_i \in \mathbb{C}^{N_p \times N^2}$ is the scattering matrix constructed for the free-space wavenumber k_{0i} at the i-th frequency and $\boldsymbol{e}_i(x_{1:N_p}, k_{0i}) \in \mathbb{C}^{N_p \times 1}$ is the corresponding scattered field measurements at N_p locations on OD and $\boldsymbol{\nu} \in \mathbb{C}^{M \times 1}$ is complex additive white Gaussian noise (AWGN).

In particular, the mn^{th} entry of the scattering matrix $\mathbf{A}_i$ is given by

$$A_i^{mn} = jk_{li}^2 \omega_i \mu_0 G^2(x_{om}, \vec{r}_n, k_{0i}) \Delta_x \Delta_z, \qquad (4)$$

where x_{om} denotes the observation points located at quota $z_o > 0$, $\vec{r}_n = (x_n, z_n)$ are the grid points within SD and Δ_x, Δ_z the uniform discretization steps. The single-frequency scattering matrices and the scattered field measurements are stacked to construct the matrix operator $\mathbf{A} \in \mathbb{C}^{M \times N^2}$ and its corresponding data vector $e \in \mathbb{C}^{M \times 1}$, with $M = N_p N_f$, and $x \in \mathbb{C}^{N^2 \times 1}$ corresponds to the discretized version of the contrast χ.

At this juncture, Σ and SD are very finely sampled, which is done for two reasons. First, dense sampling of SD is achieved so that $\mathbf{A}$ can be considered a good approximation of the scattering operator in (2). Secondly, a fine *initial* spatio-frequency grid mimics the continuous set Σ among which optimum data positions have to be selected using sensor selection procedure. In what will follow, the model in (3) is addressed as the over-sampled matrix scattering operator.

III. BRIEF DESCRIPTION OF MPME ALGORITHM

Optimizing the spatial and frequency sampling can be conveniently attacked from a more general perspective offered by the sensors selection literature [21], [29]. In principle, all possible measurement arrangements must be checked against a suitable metric that considers noise propagation in the reconstructions. This is practically unfeasible. To overcome this drawback, several greedy methods and heuristics approaches have been developed [22]–[24]. Among the greedy methods for sensors' selection, the MPME offers the best trade-off between complexity and performance [26]. Hence, it has been selected and adapted for the subsurface imaging problem.

Consider a linear inverse problem described by the matrix operator $\mathbf{B} \in \mathbb{C}^{M \times N^2}$, N^2 is fixed a priori whereas $M \gg N^2$. MPME returns a row "pruned" matrix operator $\mathbf{B}_{opt} = \mathbf{CB} \in \mathbb{C}^{M_{opt} \times N^2}$, $\mathbf{C} \in \mathbb{R}^{M_{opt} \times M}$ being the matrix extracting the rows of $\mathbf{B}$ corresponding to the selected data, such that the minimum non-zero singular value is greater than a chosen threshold γ. The number of data is reduced since $N^2 \leq M_{opt} \leq M$. Also, the noise propagation during inversion is controlled by γ that can be chosen according to worst case error variance to be tolerable in the reconstructions.

The selection of the rows is achieved one at time. Assume that $k-1$ rows have been already selected and denote $\mathbf{C}_{k-1} \in \mathbb{R}^{k-1 \times M}$ and $\mathbf{B}_{k-1} = \mathbf{C}_{k-1} \mathbf{B}$ as the relative selection matrix and pruned model, respectively. The sensor selection using MPME [26] procedure has two parts (cycles) for selecting the the k-th row, among the remaining $M - k - 1$ rows:

1) **first cycle**: when $k < N^2$, the k-th row is determined as the one which has the largest projection onto the kernel space of $\mathbf{B}_{k-1}$;
2) **second cycle**: when $k \geq N^2$, the k-th row is determined as the one which has the largest projection on the subspace corresponding to the minimum singular value $\sigma_{N^2}(\mathbf{B}_{k-1})$.

The procedure arrests when $\sigma_N^2(\mathbf{B}_k) \geq \gamma$, with the k-th current iteration representing $M_{opt} > N^2$.

IV. PROPOSED APPROACH

In this section we provide the details on modification of the MPME procedure to the subsurface imaging scenario.

The standard MPME procedure assumes the number of measurements greater than the number of unknowns ($M > N^2$). However, unless special cases, for which it is a priory known that the unknown belongs to a finite dimensional subspace, the number of unknowns in subsurface imaging is generally large. As a consequence, the selection procedure requires a high computational cost and, what is more, the condition $M_{opt} > N^2$ can be hardly fulfilled. To cope with these drawbacks, in the sequel we address the problem of reducing the dimension of the scattering matrix and to set a new stopping rule for the MPME procedure.

A. Dimensionality reduction of the unknown space

Assume that no a priori information about the unknown is available. In order to select a proper finite dimensional representation for the unknown, three factors must be taken into account: (i) the mathematical features of the relevant scattering operator which in turn reflect the geometrical parameters of the problem (i.e., SD and Σ sizes and relative arrangement and background medium properties), (ii) the type of basis functions used for transforming $\mathcal{A}$ into $\mathbf{A}$, and (iii) the degree of accuracy (approximation error) with which $\mathcal{A}$ is approximated to $\mathbf{A}$. Pixel-wise functions are usually employed because quadrature implementation to achieve discretization is very easy. However, it is known that a subset of the first singular functions of $\mathcal{A}$ is "extremal" [30], i.e., given the number of basis functions, the approximation error for the range of $\mathcal{A}$ is minimum among all finite dimensional approximations of the same finite size.

Previous arguments suggests to employ the singular vectors of the over-sampled operator $\mathbf{A}$ to reduce the dimensionality of the unknown. To this end, the SVD of $\mathbf{A}$, is first computed. Then, the model to be used for sensors' selection is obtained as:

$$\hat{\mathbf{A}}\boldsymbol{\beta} = \mathbf{AW}\boldsymbol{\beta}, \qquad (5)$$

where $\hat{\mathbf{A}} \in \mathbb{C}^{M \times \zeta}$, $\mathbf{W} = [\boldsymbol{w}_1, \boldsymbol{w}_2, \cdots, \boldsymbol{w}_\zeta] \in \mathbb{C}^{N^2 \times \zeta}$, with $\{\boldsymbol{w}_i\}_{i=1}^\zeta$ being the first ζ right singular column vectors of $\mathbf{A}$ and $\boldsymbol{\beta}$ are the expansion coefficients of x, that is $\boldsymbol{\beta} = \mathbf{W}^H x$. Note that the very fine grid used to sample SD is only needed to let the singular vectors in $\mathbf{W}$ be a good approximation of those of $\mathcal{A}$. Here, the key point is the selection of the number of singular functions to be retained, that is ζ. In some cases, the singular values exhibit a step-like behaviour and hence ζ can be naturally chosen in correspondence of the "knee" [31], [32]. Unfortunately, this does not hold true for the problem at hand. Hence, in order to select ζ, the following simple strategy is considered:

$$\zeta = \min \left(m : \frac{\sum_{i=1}^m |\sigma_i(\mathbf{A})|^2}{\sum_{i=1}^{N^2} |\sigma_i(\mathbf{A})|^2} \geq \alpha \right), \qquad (6)$$

where $0 < \alpha < 1$ sets the error committed by replacing $\mathbf{A}$ with $\hat{\mathbf{A}}$. In practice, it sufficient to set α below but close to 1 to have ζ much lower than N^2. This is because $\mathbf{A}$ approximates

a compact continuous operator and hence most of its singular value cluster to zero. Indeed, provided to keep α close to 1, the value of α does not effect the sensors' selection very much. This is because Eq. (6) retains even the projections of the unknown that cannot be actually determined when noise enters the picture. This statement essentially describes the ill-posedness of the inverse problem related to radar imaging. Other rules, different from Eq. (6), can be employed to retain a smaller number of projections. In this way the inverse problem is implicitly regularized and the problem dimensionality furthermore reduced although the level of noise is, in general, required. Since the latter is not necessarily available, we prefer to employ Eq. (6).

B. Stopping rule for the selection procedure

A significant reduction of the problem's dimension is obtained by Eq. (6). However, the retained singular values, i.e., $\{\sigma_i(\mathbf{A})\}_{i=1}^{\zeta}$, practically capture most of the singular spectrum of $\mathbf{A}$ and hence have a very large amplitude dynamic. As a consequence, ζ is still relatively large and $\hat{\mathbf{A}}$ is highly ill-conditioned. This entails that entering the second cycle (see Section III) of the MPME is not convenient. Indeed, a large number of measurement ($M_{opt} >> \zeta$) would be required to enter the second MPME cycle and to raise the minimum singular value so as to have stable inversions. This is clearly unfeasible in most cases, particularly for the one at hand. Hence, for sensors' selection, we consider only the first cycle of the MPME procedure. This also has the remarkable advantage of significantly reducing the computational burden since multiple SVD computations are no longer required to get the maximal projection on minimum eigenspace. On the other side, the usual MPME stopping rule cannot be employed since it takes place during the second cycle.

Hence, a stopping rule must be set to stop the first cycle at some point. To this end, unless there are some system constraints that fix the number of data points a priori, it is natural to take into account the effect of noise.

Say $\hat{\mathbf{A}}_k \in \mathbb{C}^{k \times \zeta}$ the scattering matrix collecting the first selected $k < \zeta$ rows of $\hat{\mathbf{A}}$ and η_0^2 the variance of the AWGN that corrupts the data. After a least square solution procedure is employed, the norm of the noise that propagates on the reconstructions is given by

$$\eta_0^2 \sum_{n=1}^{k} \frac{1}{\sigma_n^2(\hat{\mathbf{A}}_k)} = \eta_0^2 \, MF_k, \qquad (7)$$

with

$$MF_k = \sum_{n=1}^{k} \frac{1}{\sigma_n^2(\hat{\mathbf{A}}_k)}. \qquad (8)$$

acting as a noise magnification factor (MF). Note that Eq. (7) often represents the mean square error (MSE). Here, however, this is not the case since, besides the effect of noise, further error in the reconstruction appears because $\hat{\mathbf{A}}_k$ is a sub-matrix of the filtered model $\hat{\mathbf{A}}$ and does not have full column rank. A natural way to set the stopping rule is to arrest the selection procedure as soon as the noise contribution exceeds a tolerable level. This, once again requires to know the level

of noise that corrupts data. As remarked above, herein we are assuming unknown the noise features (i.e., η_0^2). Nonetheless, it is possible to estimate the noise variance, but that adds an extra burden on the overall imaging procedure. Besides, information about the unknown targets is also required since a given level of noise in the reconstructions can be tolerated for certain targets and cannot be for other types of targets. Since no information about noise and type of target is exploited in our arguments, we choose to set the stopping rule by considering the magnification factor only.

Computing Eq. (8) in principle requires to evaluate the SVD of $\hat{\mathbf{A}}_k$ for each iteration of the selection procedure. This is computationally heavy, especially as the procedure progresses and k increases. We note that:

$$MF_k = tr[(\hat{\mathbf{A}}_k^H \hat{\mathbf{A}}_k)^{-1}], \qquad (9)$$

where $tr[\cdot]$ is the trace operator. Therefore, what we need is a quick scheme to compute the inverse matrices in Eq. (9) as the selection proceeds. Since $\hat{\mathbf{A}}_k^H \hat{\mathbf{A}}_k$ is a rank-one perturbation of $\hat{\mathbf{A}}_{k-1}^H \hat{\mathbf{A}}_{k-1}$ for each k, one could think to use the Sherman-Morrison-Woodbury (SMW) formulas [33] to compute $(\hat{\mathbf{A}}_k^H \hat{\mathbf{A}}_k)^{-1}$ starting from $(\hat{\mathbf{A}}_{k-1}^H \hat{\mathbf{A}}_{k-1})^{-1}$. So that only the $(\hat{\mathbf{A}}_1^H \hat{\mathbf{A}}_1)^{-1}$ is to be computed and the needed inverse matrices can be iteratively updated by using the SMW formulas. Unfortunately, this appealing strategy cannot be followed here because $\hat{\mathbf{A}}_k^H \hat{\mathbf{A}}_k$ are singular. Therefore, we are content to find a lower bound for MF_k. In particular, it can be easily shown that:

$$MF_k \geq \frac{k}{\sum_{n=1}^{k} \sigma_n^2(\hat{\mathbf{A}}_k)} = \frac{k}{tr[\hat{\mathbf{A}}_k^H \hat{\mathbf{A}}_k]} = \tilde{M}F_k. \qquad (10)$$

Hence, the stopping rule is set by considering $\tilde{M}F_k$. It is remarked that, selecting the number of data k_{opt} as $\tilde{M}F_{k_{opt}} \geq \gamma$, cannot be considered as good option since this is somehow equivalent to know the tolerable level of noise in the reconstructions, as discussed above.

Instead, we observe that as k increases the singular values tend to cluster towards zero. This is because $\hat{\mathbf{A}}_k$ tends to approximate $\hat{\mathbf{A}}$ and the latter arises from the compact operator $\mathcal{A}$. Therefore, while k increases, at some point the denominator in Eq. (10) changes very slowly and $\tilde{M}F_k$ starts growing linearly with k. Accordingly, we set the stopping rule when $\tilde{M}F_k$ starts to exhibit such a behaviour. Say k_{opt} the corresponding iteration and denote as $\mathbf{A}_{opt} = \hat{\mathbf{A}}_{k_{opt}}$ the corresponding scattering matrix operator. Note that this is equivalent to stopping the selection procedure as soon as a further measurement leads to a negligible "further" singular value and hence to an irrelevant contribution of unknown projection on the corresponding singular vector.

Eventually, the measurement selection procedure consists of the following step:
1) Build the over-sampled model $\mathbf{A}$ according to the parameters of the problem, compute its SVD and then obtain the reduced model $\hat{\mathbf{A}}$ using the criterion in Eq. (6).
2) Select a row of $\hat{\mathbf{A}}$ in every iteration as per the first cycle of the MPME method. In details, let $\hat{\mathbf{A}}_{k-1}$ the

matrix formed by the first $(k-1)$ selected rows of $\hat{\mathbf{A}}$. The selected rows are orthonormalized by Gram-Schmidt procedure and arranged to form the columns of the matrix $\mathbf{R}_{k-1} \in \mathbb{C}^{\zeta \times k-1}$, then the projector onto the null space of $\hat{\mathbf{A}}_{k-1}$ is built as $\mathbf{P}_{k-1} = \mathbf{I} - \mathbf{R}_{k-1}\mathbf{R}_{k-1}^H$, with $\mathbf{I} \in \mathbb{C}^{\zeta \times \zeta}$ being the identity matrix.

3) The k-th row is then selected as $\max_{i \in \mathcal{I}/S_{k-1}} \|\mathbf{P}_{k-1}\mathbf{a}_i\|_2^2/\|\mathbf{a}_i\|_2$, where $\mathbf{a_i}$ is i^{th} row of $\hat{\mathbf{A}}$, $\mathcal{I}$ and S_{k-1} denotes the indices of all the rows and selected rows respectively.

4) Add the selected row and update $\hat{\mathbf{A}}_k$ and S_k.

5) Compute $\tilde{M}F_k$ and check its behaviour.

6) If $\tilde{M}F_k$ grows linearly stop selection otherwise go back to step 2.

V. INVERSION

Once the selection procedure is completed, we end up with the reduced (in size) inverse scattering matrix problem:

$$\mathbf{A}_{opt}\,\boldsymbol{\beta} = \boldsymbol{e} + \boldsymbol{\nu} = \tilde{\mathbf{e}}. \qquad (11)$$

There are various inversion methods, such as back-propagation or migration method [28], [34] or inverse filtering [14], that can be employed to find $\boldsymbol{\beta}$. In this paper we explore the reconstructions provided by two methods taken from both classes.

The first one is a truncated singular value decomposition (TSVD). The optimized matrix expressed in terms of its SVD is given by $\mathbf{A}_{opt} = \sum_{i=1}^{M_{opt}} \boldsymbol{u}_i \sigma_i \boldsymbol{v}_i^H$, where $\{\boldsymbol{u}_i\}_{i=1}^{M_{opt}}, \{\boldsymbol{v}_i\}_{i=1}^{\zeta}$ are the left and right singular vectors respectively, and $\{\sigma_i\}_{i=1}^{M_{opt}}$ the singular values arranged in descending order. The solution $\hat{\boldsymbol{x}}$ is obtained as:

$$\boldsymbol{\beta}_{TSVD} = \sum_{i=1}^{L} \left(\frac{\boldsymbol{u}_i^H \tilde{\mathbf{e}}}{\sigma_i} \right) \boldsymbol{v}_i. \qquad (12)$$

Note that in general $L \leq M_{opt}$ since the problem in general still requires to be regularized.

The alternate approach to inverse filtering is using back-propagation algorithm. Here, this is achieved by simply approximating the inverse by the adjoint operator so that:

$$\boldsymbol{\beta}_{BP} = \mathbf{A}_{opt}^H \tilde{\mathbf{e}} = \sum_{i=1}^{M_{opt}} \sigma_i \boldsymbol{u}_i^H \tilde{\mathbf{e}} \boldsymbol{v}_i. \qquad (13)$$

The adjoint inversion method simply obtains the reconstruction of the subsurface region by backpropagating the scattered field according to the background Green function. The backpropagation algorithm is very robust against noise. This can be understood by considering the SVD expansion of $\mathbf{A}_{opt}^H$ and noting that Eq. (13) can written as Eq. (12), but with the singular values appearing in the numerator rather than in the denominator. Hence, stability against noise is implicitly obtained. There is also no need for calculation of the singular values as the solution is obtained just by the multiplication of the adjoint operator. On the other side, $\boldsymbol{\beta}_{BP}$ tends to be over-regularized and hence the achievable resolution is generally lower than that provided by TSVD, unless the singular values exhibit a step-like behaviour [11].

Finally, once $\boldsymbol{\beta}$ is retrieved (by TSVD or adjoint inversion) the contrast function is retrieved as:

$$\mathbf{x}_l = \mathbf{W}\boldsymbol{\beta}_l \qquad (14)$$

with $l = TSVD, \; BP$.

In the next sections, the proposed method is applied for object detection using the measurements from:

1) Synthetic data with the subsurface region consisting of point like scatterers.

2) Experimental data with a water pipeline buried in the subsurface region.

VI. NUMERICAL RESULTS

In this section, we consider a synthetic scattering scenario to check the proposed method for subsurface imaging. By referring to the scattering scenario depicted in Fig. 1, we consider the upper half-space as free-space, and the lower has a relative permittivity of 9 with the separation interface at $z = 0$. The spatial domain within which targets are assumed to reside is set as $SD = [-1, 1] \, m \times [-2.5, -0.5] \, m$, whereas the sensors are placed at the measurement line $OD = [-1.5, 1.5] \, m$ placed at $0.1 \, m$ from the interface in the upper half-space. The frequency band of the ground penetrating radar is $300 - 800$ MHz.
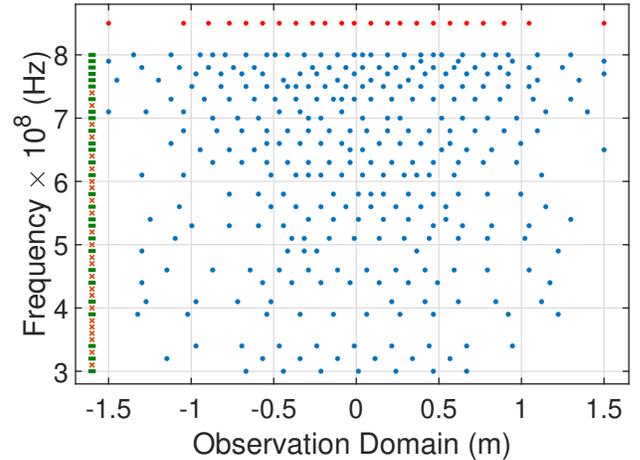

Fig. 2: Optimal spatial-frequency sensor locations (blue dots) obtained from a fine grid consisting of 6120 possible sampling points. The green dash and orange crosses denote the frequencies chosen and discarded by the algorithm, respectively. Red dots refer to the spatial positions returned by the warping method and that need to be repeated for each N_{fmin} frequencies.

To get the over-sampled matrix model, SD is discretized into 64×64 pixels, and OD is uniformly sampled with a fine sampling rate of $\lambda_{umin}/15$, with $\lambda_{umin} = 0.375 \, m$. The frequency band is sampled uniformly with a 10 MHz gap. As a result we have, $N^2 = 4096$, $N_p = 120$ and $N_f = 51$. The size of the over-sampled scattering matrix $\mathbf{A}$ is 6120×4096. The minimum number of frequencies required for subsurface imaging is given by $N_{fmin} = n(\Delta k \Delta z/\pi) = 21$, where

$\Delta k = k_{max} - k_{min}$, $\Delta z = z_{max} - z_{min}$ and n is the refractive index of the lower half-space background medium. It is worth noting that the total number of considered frequencies, N_f, is much larger than N_{fmin}. The frequency band is also finely sampled resulting in the scattering matrix $\mathbf{A}$ with fine discretization in both spatio-frequency domain. Therefore such a fine grid in both spatio-frequency domain approximates the continuous scattering operator which can be further used to run the sensor selection algorithm. Finally, in all the simulations we set $\alpha = 0.999$.
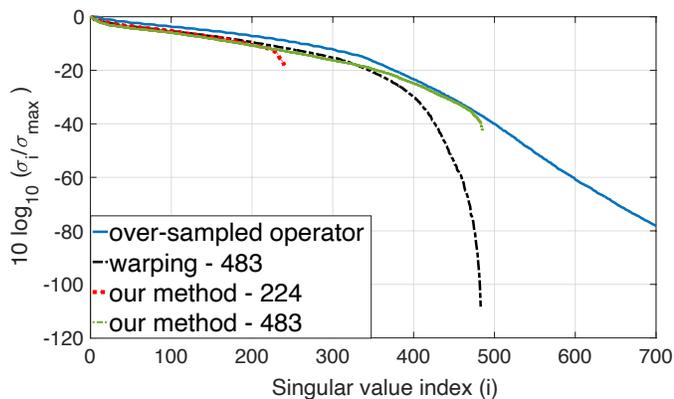

Fig. 3: Comparison of the normalized singular spectrum of the over-sampled operator, optimal matrix returned by the proposed method (with 224 and 483 measurements) and the analytical warping approach (with 483 measurements). The singular spectrum of the optimal matrix approximates the over-sampled operator better compared to the analytical warping method for the same number of measurements.

A. Warping sampling vs proposed approach

We start the analysis by comparing the proposed approach with the warping sampling method, which is the method in the literature prescribing lesser data collection. In particular, we compare our proposed method of obtaining optimal sensor locations in both frequency and spatial domain simultaneously with the analytical solution from [19]. For the described simulation setting, the optimal spatio-frequency sampling locations are shown in Fig. 2. The green dash and orange crosses denotes the frequencies chosen and discarded, respectively, by the algorithm. A total of 224 measurement locations in the spatio-frequency domain are picked by the proposed method. Instead, the number of spatial sampling locations obtained at the highest frequency using the analytical warping method is 23, which are shown as 'red' dots at the top of Fig. 2. The same locations need to be repeated for all $N_{fmin} = 21$ frequencies sampled uniformly in the bandwidth. Therefore, the warping method requires a total of 483 measurements. Hence, the proposed method reduces more than 50% of the measurements by optimizing the sensor locations in both spatio-frequency grids. In view of this data reduction, it is necessary to appreciate how the determined sensors' arrangements affect the imaging problem. Here, we start by analysing the normalized singular value behaviour shown in Fig. 3 of the over-sampled matrix $\mathbf{A}$,

optimal matrix $\mathbf{A}_{opt}$ and the matrix generated by the sensor locations obtained from warping sampling method. It is seen that the singular values corresponding to $\mathbf{A}_{opt}$ overlap very well to the first part of the singular value behaviour of the over-sampled matrix. By contrast, the singular values corresponding to the warping method are close to the singular values of $\mathbf{A}$ for a longer part. However, at some point the singular values exhibit a more quickly decay, meaning that the sensor placement arrangement provided by the warping method is not optimal. To check if the proposed method works better while increasing the number of sensors (which corresponds to relaxing the constraint onto the magnification factor) we re-run the same case by arresting the selection procedure when the number of measurements equals the one required by the warping method. It is seen from Fig. 3 that the optimal matrix with 483 measurements has a better singular value behaviour compared to warping method and approximate very well those of $\mathbf{A}$.

We conclude that the proposed procedure realizes a better selection of the measurement points than the warping method, and hence outperforms other sampling methods in the literature that warping has been shown superior to.

B. Reconstruction Examples

We turn to address some reconstruction examples. To this end, we consider three point-like scatterers located in the lower half-space at $(-0.5, -1.5)$, $(0, -2)$ and $(0.5, -1.5)$, respectively. To set the benchmark for backpropagation and TSVD reconstructions obtained by employing the data set returned by our method, we first reconstruct the three point scatterers with the entire data-set, that is, inverting $\mathbf{A}$. Additionally, we investigate the imaging of an extended target, a metallic cylindrical object with an 8-inch (≈ 20cm) diameter placed at $(0, -1.4)$. This comprehensive analysis of different scattering scenarios allows us to evaluate and compare the performance and effectiveness of our proposed approach.

Figs. 4a and 4b show the reconstruction of point scatterers (contrast) with noiseless measurements using backpropagation and TSVD methods, respectively. Figs. 4c and 4d are reconstructions for noisy measurements. The noise added to corrupt the measurements is complex additive white gaussian (AWGN) with 15 dB SNR. As anticipated, TSVD returns a sharper reconstruction than backpropagation. However, while the latter weakly depends on the noise, TSVD experiences a loss of resolution as the noise grows up due to regularization.

The reconstruction of the point scatterers using both the sampling schemes and noisy data is shown in Fig. 5. For backpropagation, the reconstructions obtained by both sampling schemes show a loss of resolution. This is expected as the regularization is very strong and is implicitly obtained by windowing of the singular values themselves. The reconstructions provided by the TSVD procedure (see Fig. 5c and 5d), has a tighter resolution. However, the proposed sampling method is definitely more convenient than warping since the required data is much lesser.

We simulate the extended target utilizing the gprMax software [35]. To achieve the subsurface imaging, we gather
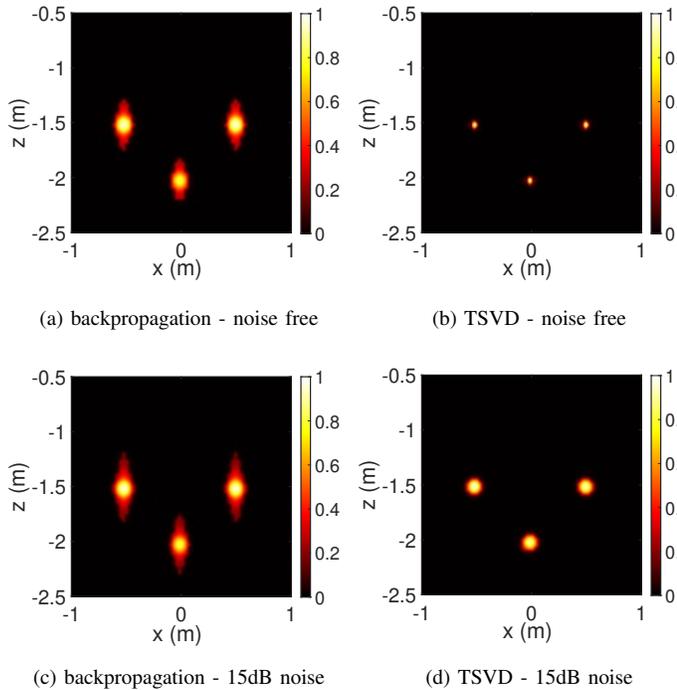
(a) backpropagation - noise free

(b) TSVD - noise free

(c) backpropagation - 15dB noise

(d) TSVD - 15dB noise

Fig. 4: Normalized contrast of point scatterers' reconstruction inverting the over-sampled operator.

(a) backpropagation - warping

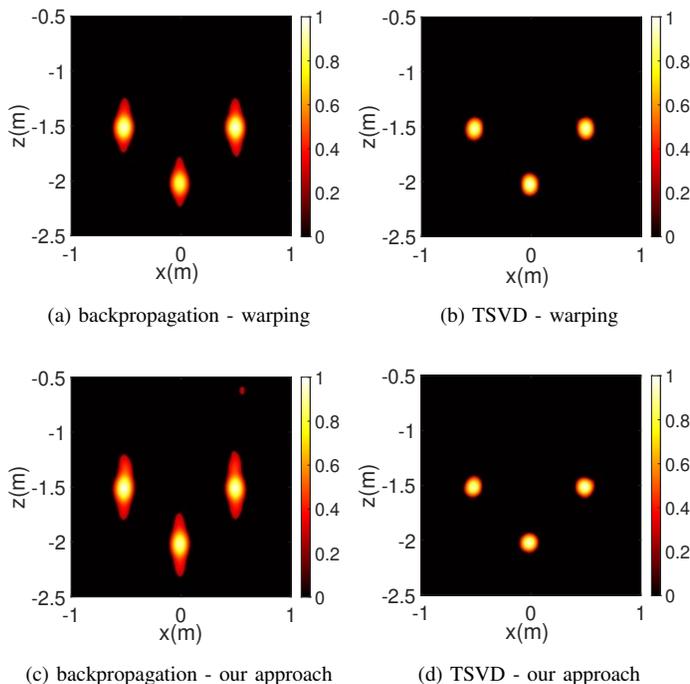(b) TSVD - warping

(c) backpropagation - our approach

(d) TSVD - our approach

Fig. 5: Normalized contrast of point scatterers' reconstruction from (a),(b) 483 locations obtained from analytical warping method; (c),(d) 224 locations provided by our method. Data are noisy with $SNR = 15dB$.

scattered field measurements at the optimal sampling locations, as illustrated in Fig. 2. The radargram, presented in Fig. 6, showcases both the raw and pre-processed (time-gated) scattered field measurements. Finally, Fig. 7 shows the reconstruction of the extended target.

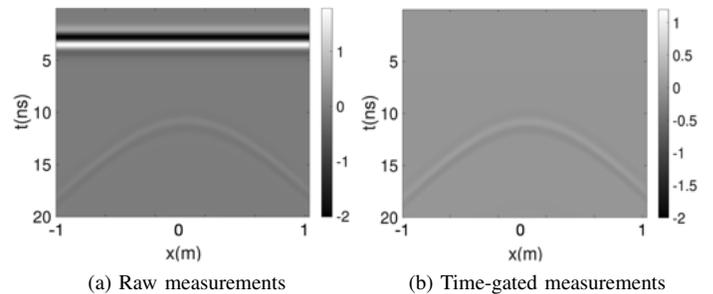(a) Raw measurements

(b) Time-gated measurements

Fig. 6: The scattered field measured at optimal locations (a) Raw measurements which includes the clutters from the GPR system and ground interface reflections, (b) Time gated measurements which removes the initial clutters. Colorbar indicates the field strength in V/m.
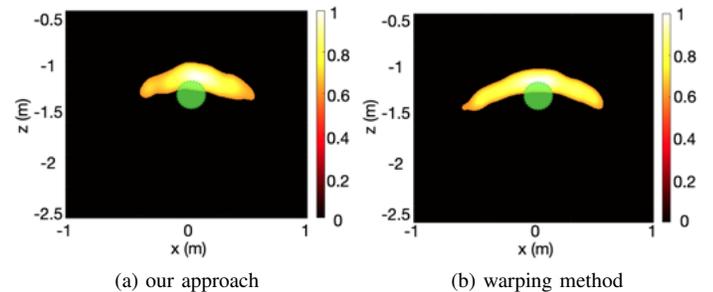

(a) our approach

(b) warping method

Fig. 7: Comparison of reconstruction of extended traget with a total of 224 vs 483 scattered field measurements. The imaging is achieved using TSVD method. The green disk indicated the position of the actual target. The measurements are corrupted 15dB SNR noise.

VII. EXPERIMENTAL RESULTS

This Section discusses the subsurface imaging in a real world setting employing the optimised sampling locations.

The experimental measurement setting is shown in Fig. 8. It is known that a water pipeline exists under the pathway leading to the fountain. In the pathway the red horizontal lines indicate the measurement domain OD. In particular, the measurements are taken over eleven different lines spread over a length of $4m$. The observation domain for each measurement line is $2.54m$. The GPR system used for the scattered field measurements emits a Ricker pulse centered at 200 MHz and the data is collected with a spatial step of $0.01m$.

The scattered field measurements for one of the measurement line (line 4) is shown in the radargram reported in Fig. 9. Raw measurements needs to be pre-processed to remove clutter from the GPR system and reflections from the ground interface. The randomness and roughness of the interface
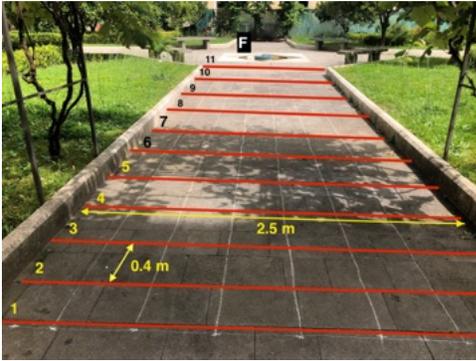
Fig. 8: Picture of the measurement site. It is the passage to the water fountain marked by an "F" in the picture.
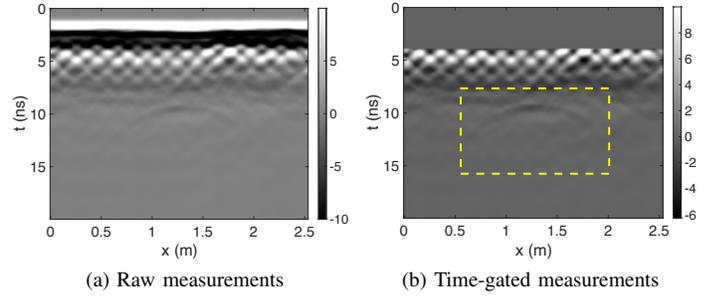

(a) Raw measurements (b) Time-gated measurements

Fig. 9: The scattered field measured at 254 locations distributed uniformly on line 4; (a) Raw measurements which includes the clutters from the GPR system and ground interface reflections, (b) Time gated measurements which removes the initial clutters. The scattered field from the pipeline is with in the dotted yellow box. Colorbar indicates the field strength in V/m

will have a minor effect on the scattering if the transmitted wavelength is relatively large. As the ground interface along the pathway changes slowly over the scanning area without any sudden dips and peaks, we see in Fig. 9a nearly constant strips of reflected signal. The pre-processed measurements are shown in Fig. 9b after clutter rejection. The literature has various methods for ground clutter rejection such as mean subtraction method [36]–[38], subspace projection method [39], etc. In this paper, we use entropy based time gating method [40], which avoids to partially filter the already weak signals coming from buried targets, as it happens for mean subtraction and subspace methods. More in detail, the entropy time gating measures the similarity of the reflected signal at each time trace over the length of measurement domain. The reflected signal is classified as clutter for a very high similarity measure. A time gating window is multiplied with each time trace of the measured signal such that the ground interface and antenna's internal reflections are eliminated.

The radargram in Fig. 9b shows that the scattered signals are mainly due to a shallow buried reinforcement grid and a pipeline supplying water to the fountain (indicated as yellow rectangle), which is almost in the centre of the pathway. The post processed data is used as the ground truth which provides information about the subsurface scatterer. The time traces are Fourier transformed for imaging purposes and frequencies within the band $100 - 725$ MHz are retained with a frequency step of 25 MHz. Moreover, scene reconstruction is pursued by a slice approach: for each measurement line a 2D slice of the scene is obtained. Then, the slices are interpolated and shown as 3D isosurface plots. For each slice, $SD = 2m \times 1.5m$ is considered and discretized into 48×48 pixels. The over-sampled model hence results 6604×2304 in size, with $N_p = 254$, $N_f = 26$ and $N^2 = 2304$.

The optimal measurement grid returned by the proposed method is shown in Fig. 10. In particular, the measurement grid was obtained by assuming for the lower half-space a relative dielectric permittivity of 3.5. The number of selected measurement points are only 210, which are picked out of 6604 possible set. The reduction of data storage is even more amazing if all the 11 slices are considered, 2300 scattered field measurements instead of 72644.

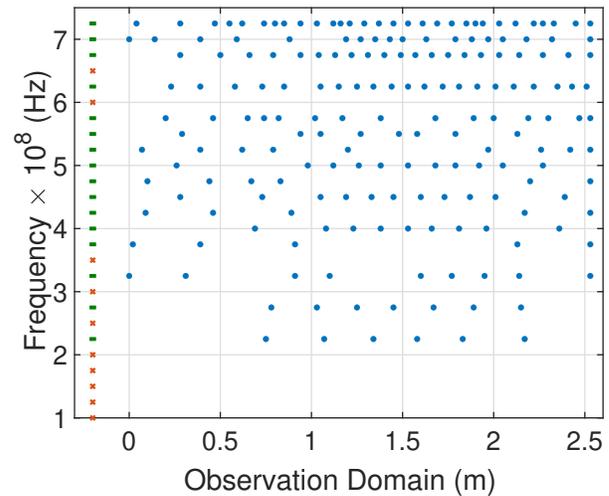We now pass to consider the reconstructions that can be

Fig. 10: Optimal spatio-frequency samples for the experimental setup. The total number of selected measurement locations are 210 out of 6604. Green mark indicates the selected frequencies whereas the red one indicates the discarded frequencies.

obtained by exploiting the selected measurements. In order to set the benchmark, we first perform the reconstruction by inverting the over-sampled model. The corresponding 3D reconstructions are reported in Fig. 11 (left). In particular, note that, as can be deduced from Fig. 9, there are two main buried targets: the shallow grid and the more deeply buried pipe. Therefore, for a clearer displaying the overall buried region is split up into two parts, the region very close to interface and the deeper subsurface part. While both bakcpropagation and TSVD allows to clearly identify the targets, as expected, the backpropagation has a lower resolution. This can be much better seen by looking at the reconstruction of the grid.

The reconstructions obtained by exploiting the optimal measurements shown in Fig. 10 are reported in Fig. 11 (right). While general considerations hold true also here, what really

matters is that the quality of reconstructions are comparable to ones in Fig. 11 (left). This definitely show the proposed data selection procedure works effectively.

Subsurface imaging over-sample vs optimal sample

(a) BP - full measurements   (b) BP - optimal measurements

(c) BP - full measurements   (d) BP - optimal measurements

(e) TSVD - full measurements   (f) TSVD - optimal measurements

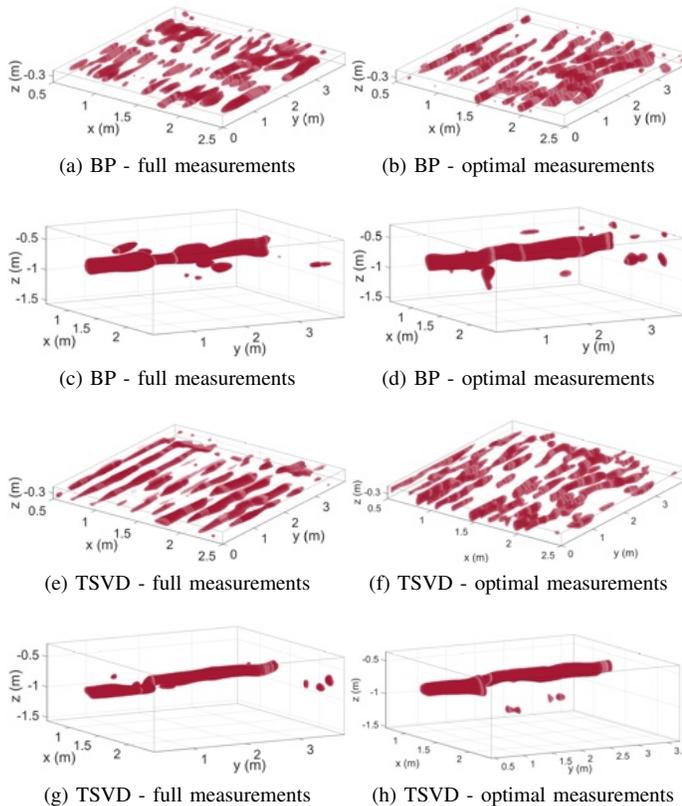(g) TSVD - full measurements   (h) TSVD - optimal measurements

Fig. 11: Comparison of reconstruction of subsurface scatterers with a total of 72644 vs 2310 scattered field measurements. Figures on the left column are reconstitution with full data whereas on right shows reconstruction with optimal data. (a)-(d) shows the reconstruction using BP method, and (e)-(h) shows the reconstruction using TSVD method. The subsurface region is split in two parts to visualize the reinforcement grid and pipe separately.

VIII. DISCUSSION AND CONCLUSIONS

In this paper, we dealt with a subsurface imaging problem under a 2D scalar geometry and a multi-monostatic/multi-frequency configuration. This simplified problem description, as is commonly done, has been exploited to get slice reconstructions of the scattering scene which has been then interpolated to provide a 3D view. Reconstructions have been obtained by employing a backpropagation algorithm and a TSVD inversion, respectively. The difference between the two algorithms in terms of the achievable performance and the effect of noise has been highlighted as well. The latter, however, can be considered as a by side result of this study, which instead was mainly concerned with devising a data sampling scheme, both in spatial and frequency domain. Indeed, the aim was to progress towards a subsurface imaging which requires

as low as possible data so to save the collection time and the needed storage resources.

The proposed sampling method is inspired by the MPME algorithm (took from sensors' selection literature) which has been properly generalized to deal with the semi-discrete inverse problem related to subsurface imaging. The latter dramatically reduces the computational burden of the standard MPME procedure. Note that no apriori information about the target, but it resides within a given spatial domain SD is assumed to achieve such a result. However, the proposed approach can further benefit from the apriori information. For example, suppose it is known that the contrast function belongs to a less general function set. In that case, the proposed algorithm can be applied to the composition between the scattering operator and the orthogonal projector onto the set the contrast is known to belong. This is expected to further reduce the number of data required to represent any field scattered by such a particular type of target.

Contrary to expectations, no symmetric data arrangement is obtained for numerical and experimental examples. Like the standard MPME, the proposed method is a greedy approach that, in order to avoid the impractical computational cost due to exhaustive searching, determines the sensing locations one by one. Accordingly, we do not know the contribution of each sensor location for the final sensor configuration; therefore, such a strategy cannot guarantee the optimal solution. Moreover, at the k-th iteration, the selected row is the one that is more orthogonal to the subspace spanned by rows retained in the previous $(k-1)$ iterations. Basically, the algorithm aims to estimate an ensemble of rows that approximates an orthogonal base to represent data. In order to guarantee that what really matters is the reciprocal distance between the points, accordingly, it can happen that the symmetric point is not the best choice. The final data arrangement is affected by the sensor location chosen at the first iteration and their total number due to the stopping rule. In particular, related to the last factor, with more and more measurements (or picking more rows), it becomes hard to maintain or approximate the orthogonality between each selected row. Accordingly, different points in frequency and spatial domain can be projected in the same way onto the subspace spanned by previously selected rows resulting in the loss of symmetry. However, what matters here is to minimize the number of data compared to the literature approaches and, the proposed approach addresses such a task very well. In fact, it was shown that the number of data can be significantly reduced as compared to data sampling criteria commonly employed, including the recently introduced warping method, without degradation of the performance in the reconstructions. Numerical and experimental data has been employed to validate our approach.

ACKNOWLEDGEMENT

This article has been accepted for publication in IEEE Transactions on Geoscience and Remote Sensing. This is the author's version which has not been fully edited and content may change prior to final publication. Citation information: DOI 10.1109/TGRS.2023.3305154

10

REFERENCES

[1] M. Pastorino and A. Randazzo, *Microwave Imaging Methods and Applications*. Artech House: Boston, MA, USA, 2018.

[2] D. J. Daniels, "Surface-penetrating radar," *Electronics & Communication Engineering Journal*, vol. 8, no. 4, pp. 165–182, 1996.

[3] P. D. Gader, M. Mystkowski, and Y. Zhao, "Landmine detection with ground penetrating radar using hidden markov models," *IEEE Transactions on Geoscience and Remote Sensing*, vol. 39, no. 6, pp. 1231–1244, 2001.

[4] D. Goodman, S. Piro, *et al.*, *GPR remote sensing in archaeology*, vol. 9. Springer, 2013.

[5] V. Schenone, A. Fedeli, C. Estatico, M. Pastorino, and A. Randazzo, "Experimental assessment of a novel hybrid scheme for quantitative gpr imaging," *IEEE Geoscience and Remote Sensing Letters*, vol. 19, pp. 1–5, 2022.

[6] A. Brancaccio, G. Leone, R. Pierri, and R. Solimene, "Experimental validation of a microwave imaging method for shallow buried target detection by under-sampled data and a non-cooperative source," *Sensors*, vol. 21, p. 5148, 2021.

[7] D. Feng, Y. Liu, X. Wang, B. Zhang, S. Ding, T. Yu, B. Li, and Z. Feng, "Inspection and imaging of tree trunk defects using gpr multifrequency full-waveform dual-parameter inversion," *IEEE Transactions on Geoscience and Remote Sensing*, vol. 61, pp. 1–15, 2023.

[8] D. L. Marks, "A family of approximations spanning the born and rytov," *Optics Express*, vol. 14, pp. 8837–8848, 2006.

[9] R. Solimene, A. Buonanno, F. Soldovieri, and R. Pierri, "Physical optics imaging of 3-d pec objects: Vector and multipolarized approaches," *IEEE Transactions on Geoscience and Remote Sensing*, vol. 48, pp. 1–15, 2009.

[10] G. Gennarelli, I. Catapano, F. Soldovieri, and R. Persico, "On the achievable imaging performance in full 3-d linear inverse scattering," *IEEE Transactions on Antennas and Propagation*, vol. 63, pp. 1150–1155, 2015.

[11] M. A. Maisto, R. Pierri, and R. Solimene, "Near-field transverse resolution in planar source reconstructions," *IEEE Transactions on Antennas and Propagation*, vol. 69, pp. 4836–4845, 2021.

[12] J. Fortuny-Guasch and J. M. Lopez-Sanchez, "Extension of the 3-d range migration algorithm to cylindrical and spherical scanning geometries," *IEEE Transactions on Antennas and Propagation*, vol. 49, pp. 1434–1444, 2001.

[13] M. A. Maisto, R. Solimene, and R. Pierri, "Transverse resolution in microwave imaging for strip objects buried in a half-space medium," *Progress In Electromagnetics Research M*, vol. 88, pp. 145–157, 2020.

[14] M. Bertero, "Linear inverse and ill-posed problems," *Adv. Electron. Electron Phys*, vol. 75, pp. 539–545, 1989.

[15] M. Soumekh, "A system model and inversion for synthetic aperture radar imaging," *IEEE Transactions on Image Processing*, vol. 1, pp. 64–76, 1992.

[16] M. Soumekh, "Depth-focused interior echo imaging," *IEEE Transactions on Image Processing*, vol. 8, pp. 1608–1618, 1999.

[17] J. M. Lopez-Sanchez and J. Fortuny-Guasch, "3-d radar imaging using range migration techniques," *IEEE Transactions on Antennas and Propagation*, vol. 48, pp. 728–737, 2000.

[18] M. A. Maisto, R. Pierri, and R. Solimene, "Spatial sampling in monostatic radar imaging," *IEEE Geoscience and Remote Sensing Letters*, vol. 19, pp. 1–5, 2022.

[19] M. A. Maisto, R. Pierri, and R. Solimene, "Sensor arrangement in monostatic subsurface radar imaging," *IEEE Open Journal of Antennas and Propagation*, vol. 2, pp. 3–13, 2021.

[20] M. A. Maisto, M. Masoodi, R. Pierri, and R. Solimene, "Sensor arrangement in through-the wall radar imaging," *IEEE Open Journal of Antennas and Propagation*, vol. 3, pp. 333–341, 2022.

[21] S. J. Reeves and L. P. Heck, "election of observations in signal reconstruction," *IEEE Transactions on Signal Processing*, vol. 43, no. 2, pp. 788–791, 1995.

[22] S. Joshi and S. Boyd, "Sensor selection via convex optimization," *IEEE Transactions on Signal Processing*, vol. 57, no. 2, pp. 451–462, 2008.

[23] M. Naeem, S. Xue, and D. C. Lee, "Cross-entropy optimization for sensor selection problems," in *2009 9th International Symposium on Communications and Information Technology*, pp. 396–401, IEEE, 2009.

[24] J. Ranieri, A. Chebira, and M. Vetterli, "Near-optimal sensor placement for linear inverse problems," *IEEE Transactions on signal processing*, vol. 62, pp. 1135–1146, 2014.

[25] L. Yao, W. A. Sethares, and D. C. Kammer, "Sensor placement for on-orbit modal identification via a genetic algorithm," *AIAA journal*, vol. 31, no. 10, pp. 1922–1928, 1993.

[26] C. Jiang, Y. C. Soh, and H. Li, "Sensor placement by maximal projection on minimum eigenspace for linear inverse problems," *IEEE Transactions on Signal Processing*, vol. 64, pp. 5595–5610, 2016.

[27] Y. Wang and W. C. Chew, "An iterative solution of the two-dimensional electromagnetic inverse scattering problem," *International Journal of Imaging Systems and Technology*, vol. 1, no. 1, pp. 100–108, 1989.

[28] A. J. Devaney, *Mathematical foundations of imaging, tomography and wavefield inversion*. Cambridge University Press, 2012.

[29] L. P. Heck, "Broadband sensor and actuator selection for active control of smart structures," in *Proc. SPIE 2442, Smart Structures and Materials 1995: Mathematics and Control in Smart Structures*, SPIE, 1995.

[30] D. Jagerman, "ϵ-entropy and approximation of bandlimited functions," *SIAM Journal on Applied Mathematics*, vol. 17, pp. 362–377, 1969.

[31] R. Piestun and D. A. B. Miller, "Electromagnetic degrees of freedom of an optical system," *Journal of the Optical Society of America A*, vol. 17, pp. 892–902, 2000.

[32] R. Solimene, M. A. Maisto, G. Romeo, and R. Pierri, "On the singular spectrum of the radiation operator for multiple and extended observation domains," *International Journal of Antennas and Propagation*, vol. 2013, pp. 1–10, 2013.

[33] W. W. Hager, "Updating the inverse of a matrix," *SIAM Review*, vol. 31, pp. 221–239, 1989.

[34] F. Soldovieri, R. Solimene, and F. Ahmad, "Sparse tomographic inverse scattering approach for through-the-wall radar imaging," *IEEE Transactions on Instrumentation and Measurement*, vol. 61, pp. 3340–3350, 2012.

[35] C. Warren, A. Giannopoulos, and I. Giannakis, "gprmax: Open source software to simulate electromagnetic wave propagation for ground penetrating radar," *Computer Physics Communications*, vol. 209, pp. 163–170, 2016.

[36] T. Gebremichael, D. Mali, A. M. Zoubir, *et al.*, "Clutter reduction techniques for gpr based buried landmine detection," in *2011 International Conference on Signal Processing, Communication, Computing and Networking Technologies*, pp. 182–186, IEEE, 2011.

[37] R. Persico and F. Soldovieri, "Effects of background removal in linear inverse scattering," *IEEE Transactions on Geoscience and Remote Sensing*, vol. 46, no. 4, pp. 1104–1114, 2008.

[38] M. Dehmollaian, M. Thiel, and K. Sarabandi, "Through-the-wall imaging using differential sar," *IEEE transactions on geoscience and remote sensing*, vol. 47, no. 5, pp. 1289–1296, 2009.

[39] U. S. Khan and W. Al-Nuaimy, "Background removal from gpr data using eigenvalues," in *Proceedings of the XIII Internarional Conference on Ground Penetrating Radar*, pp. 1–5, IEEE, 2010.

[40] R. Solimene, A. Cuccaro, A. Dell'Aversano, I. Catapano, and F. Soldovieri, "Ground clutter removal in gpr surveys," *IEEE Journal of Selected Topics in Applied Earth Observations and Remote Sensing*, vol. 7, no. 3, pp. 792–798, 2013.